Stability and Instability of Time-Domain Boundary Element Methods for the Acoustic Neumann Problem

Simon Schneider[1,3*], **Ceyhun Özdemir**[2], **Heiko Gimperlein**[2], **Karsten Urban**[1], and **Bernd Graf**[3]

[1] Institute of Numerical Mathematics, University of Ulm, Germany
[2] Engineering Mathematics, University of Innsbruck, Austria
[3] Structural Mechanics and Acoustics, Ulm University of Applied Sciences, Germany

This work presents a stable time-domain boundary element method for the acoustic wave equation in three-dimensional unbounded domains. Other formulations of time-domain boundary element methods based on retarded potential operators are known to exhibit stability issues, which often hinder their use in industrial contexts. We have investigated the stability properties of a Galerkin first-kind boundary integral formulation for sound emission problems, where well-posedness can be established in both the continuous and the discrete setting. Numerical experiments confirm the accuracy and convergence of the method. We assess long-time stability through extensive simulations focusing on fine temporal resolutions and large time ranges. The proposed formulation is compared with two alternative approaches used in practice: a space-time single-layer potential approach and a semi-discretized collocation method.

1 Introduction

In many real-world applications, structural vibrations represent a significant source of airborne sound generation. With increasingly stringent noise regulations, the analysis of Noise, Vibration, and Harshness (NVH) has emerged as a distinct engineering discipline, focusing on both structure-borne and airborne noise emissions. In recent years, it has become state of the art to compute structural sound radiation directly in the time domain in a stable and efficient manner [1], leading to growing interest in time-domain simulations of sound propagation. The time-domain Boundary Element Method (TDBEM) offers an attractive approach in this context, as it reduces the spatial dimension of the problem by one and thus requires discretization only of the vibrating surface. This results in a considerably simpler discretization process—an important advantage that enhances practical applicability, especially for small and medium-sized enterprises. However, it is well known that time-domain boundary element methods are often hindered by stability issues, which has so far limited their widespread adoption in industrial applications. To address these challenges, we propose a stable space-time discretization of the hypersingular operator. Employing a Galerkin framework, the method provides accurate and reliable results over extended time periods, making it especially well-suited for industrial simulations with transient excitation signals. Although highly relevant in practice, the long-time behavior and stability of the numerical method remains insufficiently explored in existing literature. To close this gap, we investigate the stability of the proposed formulation over extended time intervals with fine time steps. For comparison, we consider two widely used practical approaches: a space-time second-kind integral equation and a collocation-based method utilizing a time-stepping scheme. More specifically, we consider the sound radiation of a vibrating structure Ω with boundary $\Gamma = \partial\Omega$ in the acoustic domain $\mathbb{R}^3\backslash\overline{\Omega}$ by the following Neumann problem:

$$\frac{1}{c^2}\frac{\partial^2 u}{\partial \tau^2}(\tau, x) - \Delta u(\tau, x) = 0 \quad \text{in } \mathbb{R}^+ \times \mathbb{R}^3\backslash\overline{\Omega} \tag{1a}$$

$$u(\tau, x) = \frac{\partial u}{\partial \tau}(\tau, x) = 0 \quad \text{in } \mathbb{R}_0^- \times \mathbb{R}^3\backslash\overline{\Omega} \tag{1b}$$

$$\frac{\partial u}{\partial n}(\tau, x) = f(\tau, x) \quad \text{in } \mathbb{R}^+ \times \Gamma \tag{1c}$$

We represent the time by τ, the speed of sound by $c = 343$ m/s, and by ρ the density of the medium air. The radiated acoustic pressure field is is given by the solution of $u(\tau, x)$. The boundary condition $f(\tau, x)$ on Γ (see Eq. (1c)) describes the coupling between structural vibrations and the acoustic field:

$$f(\tau, x) = \rho \frac{\partial^2 s_n}{\partial \tau^2}(\tau, x).$$

Here, $s_n(\tau, x)$ is the normal component of the structural displacement, whose second derivative with respect to time acts as a source term for the radiated pressure and corresponds to the structure-borne noise at the surface.
Our work contributes to the recent wider interests in boundary element methods for wave equations, see [2, 3, 18] for an

* Corresponding author: Simon.Schneider@thu.de

overview of both Galerkin and convolution quadrature methods. The rigorous mathematical analysis of time-domain Galerkin boundary element methods was initiated by Bamberger and Ha-Duong [4], with recent contributions to the analysis and stability in [5]. Their algorithmic aspects, including the marching-on-in-time time stepping schemes and the efficient assembly of the Galerkin matrix, were thoroughly studied by Terrasse [6] and by Ostermann, Maischak and Stephan [10, 11]. For a detailed discussion we refer the reader to Ostermann's dissertation [12]. We further note relevant recent works including the efficient assembly and compression of the space-time matrices for both time-stepping and more general space-time discretizations [7–9].

2 Time Domain Boundary Integral Formulation for Sound Emission

To simplify the equations, we introduce a scaled time variable $t = c\,\tau$:

$$\frac{\partial^2 u}{\partial t^2}(t,x) - \Delta u(t,x) = 0 \quad \text{in } \mathbb{R}^+ \times \mathbb{R}^3 \setminus \overline{\Omega}, \tag{2a}$$

$$u(t,x) = \frac{\partial u}{\partial t}(t,x) = 0 \quad \text{for } t < 0,\ x \in \mathbb{R}^3 \setminus \overline{\Omega}, \tag{2b}$$

$$\frac{\partial u}{\partial n}(t,x) = f(t,x) \quad \text{on } \mathbb{R}^+ \times \Gamma. \tag{2c}$$

We start from a double-layer potential representation of $u(t,x)$:

$$u(t,x) = D\psi(t,x) := \int_{\mathbb{R}^+} \int_\Gamma \frac{\partial G}{\partial n_y}(t-\tau,x,y)\psi(\tau,y)d\tau ds_y. \tag{3}$$

which defines u in the exterior domain $\mathbb{R}^+ \times \mathbb{R}^3 \setminus \overline{\Omega}$ as the action of the retarded double-layer operator D on the unknown acoustic density ψ. Applying the trace theorem together with the normal derivative operator ∂_n, we obtain from (3) the first-kind boundary integral equation:

$$\mathcal{W}\psi(t,x) = \partial_n u(t,x) = f(t,x) \quad \text{on } \mathbb{R}^+ \times \Gamma. \tag{4}$$

The hypersingular operator $\mathcal{W}$ is defined by:

$$\mathcal{W}\psi := \int_{\mathbb{R}^+} \int_\Gamma \frac{\partial^2 G}{\partial n_x \partial n_y}(t-\tau,x,y)\,\psi(\tau,y)\,d\tau\,ds_y \tag{5}$$

where the potential operators are based upon the fundamental solution G of the wave equation in $\mathbb{R}^3$:

$$G(t-\tau,x,y) = \frac{\delta\big(t-\tau-\|x-y\|\big)}{4\pi\|x-y\|}.$$

For the analysis of well-posedness, i.e., the mapping properties of time-dependent boundary integral operators, we introduce space–time anisotropic Sobolev spaces defined on the boundary $\Gamma \subset \mathbb{R}^3$ [4, 15]. In the case that Γ is a flat screen in $\mathbb{R}^3$, we choose $\sigma > 0$ and $s, r \in \mathbb{R}$. Then the anisotropic Sobolev space $H^s_\sigma(\mathbb{R}^+, H^r(\Gamma))$ consists of distributions ϕ on $\mathbb{R}^+ \times \Gamma$ that vanish at $t = 0$. This space is equipped with the norm

$$\|\phi\|_{s,r,\Gamma} := \left(\int_{\mathbb{R}} \int_{\mathbb{R}^2} |\omega+i\sigma|^{2s} \big(|\omega+i\sigma|^2 + |\xi|^2\big)^r \, |\mathcal{F}\phi(\omega+i\sigma,\xi)|^2 \, d\xi\, d\omega \right)^{1/2},$$

where $\mathcal{F}\phi$ denotes the Fourier–Laplace transform of ϕ in time and space and $\omega \in \mathbb{C}\backslash\{0\}$. The weighted Sobolev spaces and their associated norms can also be defined on general Lipschitz boundaries Γ; see, e.g., [20], [13].
The weak formulation of (5) is based on the bilinear form

$$w(\psi,\Psi) := \int_{\mathbb{R}^+\times\Gamma} (\mathcal{W}\psi)(t,x)\,\partial_t\Psi(t,x)\,d_\sigma t\,ds_x, \tag{6}$$

where we use the weighted measure $d_\sigma t := e^{-2\sigma t}dt$.

Theorem 2.1 *Let $r \in \mathbb{R}$. The hypersingular operator $\mathcal{W}$ and its inverse $\mathcal{W}^{-1}$ are continuous mappings:*

$$\mathcal{W} : H^{r+1}_\sigma(\mathbb{R}^+, H^{\frac{1}{2}}(\Gamma)) \to H^r_\sigma(\mathbb{R}^+, H^{-\frac{1}{2}}(\Gamma)),$$
$$\mathcal{W}^{-1} : H^{r+1}_\sigma(\mathbb{R}^+, H^{-1/2}(\Gamma)) \to H^r_\sigma(\mathbb{R}^+, H^{1/2}(\Gamma)).$$

Moreover, $w(\cdot,\cdot)$ is weakly coercive, i.e.,

$$w(\psi,\psi) \geq C(\sigma)\|\psi\|^2_{0,\frac{1}{2},\Gamma,*}.$$

The proofs, as presented for example in [18] or [21], rely on the use of the Fourier–Laplace transform.
We define the variational formulation of (4):
Find $\psi \in H^1_\sigma(\mathbb{R}^+, H^{1/2}(\Gamma))$ such that for all $\Psi \in H^1_\sigma(\mathbb{R}^+, H^{1/2}(\Gamma))$:

$$w(\psi, \Psi) = \int_{\mathbb{R}^+ \times \Gamma} f \partial_t \Psi \, d_\sigma t \, ds_x \tag{7}$$

as well as its Galerkin approximation in a finite-dimensional subspace $V \subset H^1_\sigma(\mathbb{R}^+, H^{1/2}(\Gamma))$:
Find $\psi_{\Delta t,h} \in V$ such that for all $\Psi_{\Delta t,h} \in V$:

$$w(\psi_{\Delta t,h}, \Psi_{\Delta t,h}) = \int_{\mathbb{R}^+ \times \Gamma} f_{\Delta t,h} \partial_t \Psi_{\Delta t,h} \, d_\sigma t \, ds_x. \tag{8}$$

Corollary 2.2 *Let $g \in H^2_\sigma(\mathbb{R}^+, H^{-1/2}(\Gamma))$ and let $\psi \in H^1_\sigma(\mathbb{R}^+, \widetilde{H}^{1/2}(\Gamma))$ denote the unique solution of* (7)*, and $\psi_{\Delta t,h} \in V$ the unique solution of* (8)*. Then, the following stability estimates hold:*

$$\|\psi\|_{1,\frac{1}{2},\Gamma} \leq C \|g\|_{2,-\frac{1}{2},\Gamma}, \quad \|\psi_{\Delta t,h}\|_{1,\frac{1}{2},\Gamma} \leq C \|g\|_{2,-\frac{1}{2},\Gamma}.$$

Remark 2.3 Alternative formulations based upon the single-layer potential S and the adjoint double-layer operator $\mathcal{K}'$ lead to second-kind boundary integral equations such as $(-\mathrm{Id} + \mathcal{K}')\varphi = g$ (see [16]). While well-posedness in anisotropic Sobolev spaces is established [18], the lack of coercivity may lead to unstable numerical schemes. In practice, collocation methods based on the representation formula are frequently used due to their simplicity [17], and were extensively studied in the 1990s, for example by P.J. Davies and D.B. Duncan. However, these methods often exhibit stability issues and are therefore not well suited for robust industrial simulations.

3 Discretization and Algorithmic Considerations

3.1 Discretization

We approximate Γ by $\bigcup_{i=1}^{N_s} \Gamma_i$, a quasi-uniform mesh $\mathcal{T}_s$ with triangles Γ_i. For the time discretization, we divide $\mathbb{R}^+$ uniformly into subintervals $I_n = (t_{n-1}, t_n]$ of size Δt, forming the time mesh $\mathcal{T}_t$. We use polynomial basis functions $\{\varphi_i^p\}$ of degree p on $\mathcal{T}_S$ and $\{\beta_n^q\}$ of degree q on $\mathcal{T}_T$, and define the discrete spaces:

$$V_h^p = \{\phi : \Gamma \to \mathbb{R} : \ \phi|_{\Gamma_i} \in \mathbb{P}^p, \text{ continuous and } \phi|_{\partial\Gamma} = 0 \text{ if } p \geq 1\},$$
$$V_{\Delta t}^q = \{\Phi : \mathbb{R}^+ \to \mathbb{R} : \ \Phi|_{I_n} \in \mathbb{P}^q, \text{ continuous and } \Phi(0) = 0 \text{ if } q \geq 1\}.$$

The discrete approximation space is defined as the tensor product

$$V_{\Delta t,h}^{p,q} = V_h^p \otimes V_{\Delta t}^q,$$

associated with the space-time mesh $\mathcal{T}_{S,T} = \mathcal{T}_T \times \mathcal{T}_S = \bigcup_{n,i} \square_{n,i}$. Each space–time element is given by $\square_{n,i} = I_n \times \Gamma_i$ and is characterized by the element size $H_{n,i}$. A basis of $V_{\Delta t,h}^{p,q}$ is given by the tensor products of the basis functions $\beta_n^q(t)$ and $\varphi_i^p(x)$.
Using the subspace $V_{\Delta t,h}^{1,1} \subset H^1_\sigma(\mathbb{R}^+, \tilde{H}^{-1/2}(\Gamma))$. the ansatz functions take the form:

$$\psi_{\Delta t,h}(t,x) = \sum_{m=1}^{N_t} \sum_{i=1}^{N_s} c_i^m \varphi_i^1(x) \beta_m^1(t), \tag{9}$$

where $\beta_m^1(t) = (\Delta t)^{-1} \big((t - t_{m-1})\gamma^m(t) - (t - t_{m+1})\gamma^{m+1}(t)\big)$, and $\gamma^j(t)$ denotes the characteristic function of I_j. For the implementation, it is convenient to use test functions of the form:

$$\dot{\Psi}_{\Delta t,h}(t,x) = \varphi_j^1(x)\dot{\gamma}^n(t), \quad j = 1, \ldots, N_s, \quad n = 1, \ldots, N_t. \tag{10}$$

3.2 Implementation of $\mathcal{W}$

The implementation follows the approach presented in [14]. For simplicity, we set $\sigma = 0$ for calculations and introduce the retarded time $t' = t - |x - y|$. Based upon the representation of the hypersingular operator $\mathcal{W}$ in (5), we get for the left-hand side of (8):

$$\int_{\mathbb{R}^+ \times \Gamma} (\mathcal{W}\psi) \, \partial_t \Psi \, dt \, ds_x = \frac{1}{2\pi} \int_0^\infty \int_{\Gamma \times \Gamma} \Big\{ \frac{-n_x \cdot n_y}{|x-y|} \dot{\psi}(t', y) \ddot{\Psi}(t, x) + \frac{(\mathrm{curl}_{|\Gamma} \, \psi)(t', y) \cdot (\mathrm{curl}_{|\Gamma} \, \dot{\Psi})(t, x)}{|x-y|} \Big\} ds_y \, ds_x \, dt. \tag{11}$$

By using the discrete representation (9) and (10) we obtain:

$$\int_{\mathbb{R}^+\times\Gamma} \mathcal{W}\psi_{\Delta t,h}(t,x)\,\partial_t\Psi_{\Delta t,h}(t,x)\,dt\,ds_x = A - B,$$

with

$$A = \sum_{m=1}^{N_t}\sum_{i=1}^{N_s}\frac{c_i^m}{2\pi}\int_{\Gamma\times\Gamma}\frac{n_x\cdot n_y}{|x-y|}\varphi_i^1(y)\varphi_j^1(x)\left(\int_0^\infty \dot\beta_1^m(t')\dot\gamma^n(t)\,dt\right)ds_y\,ds_x,$$

and

$$B = \sum_{m=1}^{N_t}\sum_{i=1}^{N_s}\frac{c_i^m}{2\pi}\int_{\Gamma\times\Gamma}\frac{1}{|x-y|}\int_0^\infty \beta_1^m(t')\ \mathrm{curl}_{|\Gamma}\,\varphi_i^1(y)\,\gamma^n(t)\ \mathrm{curl}_{|\Gamma}\,\varphi_j^1(x)\,dt\,ds_y\,ds_x.$$

With the Dirac distribution δ_{t_n} and $\dot\gamma^n = \delta_{t_{n-1}} - \delta_{t_n}$, we obtain for the inner time integral in A:

$$\int_0^\infty \dot\beta_1^m(t')\dot\gamma^n(t)dt = -(\Delta t)^{-1}\left(\chi_{E_{n-m}}(x,y) - 2\chi_{E_{n-m-1}}(x,y) + \chi_{E_{n-m-2}}\right).$$

Here, E_l denotes a light cone, defined as $E_l := \{(x,y)\in\Gamma\times\Gamma : t_l \le |x-y| \le t_{l+1}\}\subset\Gamma\times\Gamma$ and the indicator function $\chi_{E_l}(x,y)$, which is equal 1 if $(x,y)\in E_l$, and 0 otherwise. Thus, we conclude

$$\begin{aligned} A = \sum_{m=1}^{N_t}\sum_{i=1}^{N_s} c_i^m\Bigg[&-\int_{E_{n-m}}\frac{(n_x\cdot n_y)(\Delta t)^{-1}\varphi_i^1(y)\varphi_j^1(x)}{2\pi|x-y|}ds_y\,ds_x \\ &+2\int_{E_{n-m-1}}\frac{(n_x\cdot n_y)(\Delta t)^{-1}\varphi_i^1(y)\varphi_j^1(x)}{2\pi|x-y|}ds_y\,ds_x \\ &-\int_{E_{n-m-2}}\frac{(n_x\cdot n_y)(\Delta t)^{-1}\varphi_i^1(y)\varphi_j^1(x)}{2\pi|x-y|}ds_y\,ds_x\Bigg]. \end{aligned} \tag{12}$$

Rearranging the terms in B, we obtain:

$$B = \sum_{m=1}^{N_t}\sum_{i=1}^{N_s}\frac{c_i^m}{2\pi}\int_{\Gamma\times\Gamma}\frac{1}{|x-y|}\,\mathrm{curl}_{|\Gamma}\,\varphi_i^1(y)\,\mathrm{curl}_{|\Gamma}\,\varphi_j^1(x)\int_0^\infty \beta_1^m(t')\gamma^n(t)\,dt\,ds_y\,ds_x\,.$$

By substituting the definition of β_1^m, the time integral becomes:

$$\begin{aligned} &\int_0^\infty \beta_1^m(t')\gamma^n(t)\,dt \\ &\quad= (2\Delta t)^{-1}(|x-y|^2 - 2|x-y|t_{n-m+1} + t_{n-m+1}^2)\chi_{E_{n-m}}(x,y) \\ &\qquad+ (2\Delta t)^{-1}(|x-y|^2 - 2|x-y|t_{n-m-2} + t_{n-m-2}^2)\chi_{E_{n-m-2}}(x,y) \\ &\qquad+ (2\Delta t)^{-1}((-2|x-y|^2 + 2|x-y|(t_{n-m}+t_{n-m-1}) - (t_{n-m}^2 + t_{n-m-1}^2) + 2(\Delta t)^2) \\ &\qquad\chi_{E_{n-m-1}}(x,y) \quad =: \Upsilon^{n-m}(x,y)\,. \end{aligned}$$

Therefore we get:

$$B = \sum_{m=1}^{N_t}\sum_{i=1}^{N_s}\frac{c_i^m}{2\pi}\int_{\Gamma\times\Gamma}\frac{1}{|x-y|}\,\mathrm{curl}_{|\Gamma}\,\varphi_i^1(y)\,\mathrm{curl}_{|\Gamma}\,\varphi_j^1(x)\,\Upsilon^{n-m}(x,y)\,ds_y\,ds_x. \tag{13}$$

In summary, both terms A and B can be expressed as integrals over the light cones E_{n-m}, E_{n-m-1}, and E_{n-m-2}, associated with the m-th ansatz and the n-th test function in time. The inner integrals in (12) and (13) are evaluated using a composite hp-quadrature, while the outer integrals are computed via standard Gauss quadrature; see [10, 12]. Due to causality, the terms in A and B vanish for $t_n > t_m$. For bounded surfaces Γ, the light cone contributions E_l become zero for $l > \lceil \mathrm{diam}(\Gamma)/\Delta t\rceil$. Hence, we obtain the following discrete space-time system:

$$\underbrace{\begin{pmatrix} W^0 & 0 & 0 & 0 & \cdots \\ W^1 & W^0 & 0 & 0 & \\ W^2 & W^1 & W^0 & 0 & \\ W^3 & W^2 & W^1 & W^0 & \cdots \\ \vdots & & & \vdots & \ddots \end{pmatrix}}_{=:\boldsymbol{W}\in\mathbb{R}^{N_tN_s\times N_tN_s}} \underbrace{\begin{pmatrix} \boldsymbol{c}^0 \\ \boldsymbol{c}^1 \\ \vdots \\ \boldsymbol{c}^{N_t-1} \end{pmatrix}}_{=:\boldsymbol{C}\in\mathbb{R}^{N_tN_s}} = \underbrace{\begin{pmatrix} \boldsymbol{f}^0 \\ \boldsymbol{f}^1 \\ \vdots \\ \boldsymbol{f}^{N_t-1} \end{pmatrix}}_{=:\boldsymbol{F}\in\mathbb{R}^{N_tN_s}}. \tag{14}$$

The system matrix $\boldsymbol{W}$ exhibits a lower block Toeplitz structure with blocks $W^m \in \mathbb{R}^{N_s \times N_s}$, whose entries are assembled from A and B defined in equations (12) and (13). The coefficient vectors $\boldsymbol{c}^m = (c_1^m, \ldots, c_{N_s}^m)$ represent the discrete solution at the m-th time step. The right-hand side vectors:

$$\boldsymbol{f}^m = \frac{\Delta t}{2} \boldsymbol{I} \left(f^{m-1} + f^m \right)$$

are obtained from (8), where $\boldsymbol{I}$ is the spatial mass matrix.

3.3 Marching-on-in-time (MOT) scheme

The block lower triangular structure of the space-time system matrix $\boldsymbol{W}$ in (14), combined with the invertibility of the diagonal blocks W^0, leads to an efficient explicit solution strategy using a block forward substitution. This yields the classical MOT algorithm, where the solution coefficients $\boldsymbol{c}^n$ at time step n are computed recursively by

$$W^0 \boldsymbol{c}^n = \boldsymbol{f}^n - \sum_{m=1}^{n-1} W^{n-m} \boldsymbol{c}^m.$$

Remark 3.1 A comprehensive description of the assembly procedure for the adjoint double-layer operator K' and the corresponding right-hand side can be found in [16]. The use of piecewise constant basis functions in both space and time significantly reduces the computational complexity of matrix assembly. The resulting system matrix closely resembles that of the operator $\mathcal{W}$, enabling an analogous implementation of the MOT scheme.
A similar block-lower-triangular structure arises also in collocation-based formulations [17].

4 Validation of Sound Emissions Using an Analytical Model

To assess the accuracy of the computed sound pressure, we compare the numerical results to a known analytical solution for a vibrating unit sphere in $\mathbb{R}^3$. This exact solution, derived from retarded boundary integral equations, serves as a benchmark to evaluate the convergence and overall quality of the proposed method [19]. We start from the classical wave equation for radially symmetric functions in the $\mathbb{R}^3$:

$$\Box u = \frac{\partial^2 u}{\partial t^2} - \frac{\partial^2 u}{\partial r^2} - \frac{1}{r} \frac{\partial u}{\partial r} = 0.$$

The general radial solution $u(t, r = |x|)$ of this problem has the form $u(t, r) = \frac{1}{r} \left(\phi(r + t) + \psi(r - t) \right)$, where ϕ and ψ are functions determined by initial conditions [19].
Considering the radially symmetric Cauchy problem: $\Box u = 0, \quad u|_{t=0} = u_0(|x|), \quad \left.\frac{\partial u}{\partial t}\right|_{t=0} = u_1(|x|)$, we hence obtain for the general solution:

$$u(t, x) = \frac{1}{2r}((r + t)u_0(r + t) + (r - t)u_0(r - t)) + \frac{1}{2r} \int_{r-t}^{r+t} s u_1(s) ds.$$

For the numerical experiments we choose $u_1(|x|) = 0$, and $u_0(s) = \Big(1 + \cos(\pi s/R)\Big)^2 H(R - |s|)$, leading to

$$u(t, r) = \frac{(r - t)}{2r} \Big(1 + \cos(\pi(r - t)/R)\Big)^2 H(R - |r - t|), \tag{15}$$

where H is the Heaviside function. The corresponding Neumann data on the unit sphere are given by:

$$f = \frac{\partial}{\partial r} u(t, r)|_{r=1}. \tag{16}$$

In [19], Veit derived an explicit expression for the exact solution of (4) for radially symmetric data:

$$\psi(t) = -2 \int_0^t f(t - t') \cosh(t') dt' + \sum_{k=1}^{t/2} \sum_{l=1}^{k} (-1)^{k+1} \int_{2k}^{t} c_{k,l} (t' - 2k)^{k-l+1} e^{t'-2k} f'(t - t') dt'.$$

Here $c_{k,l}$ is given by $c_{k,l} = \binom{k-1}{l-1} \frac{2^{k-l}}{(k-l+1)!}$. We consider the solution for $R = 0.9$ for times up to $T = 10$. Six different space-time discretizations were used. The spatial mesh of the sphere was refined five times, from 20 to 20,480 elements (12

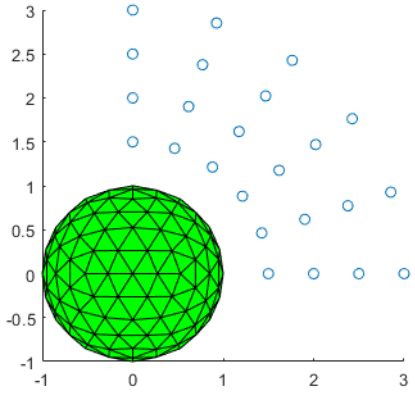

Fig. 1: Sphere with 320 triangles and 24 microphone positions.

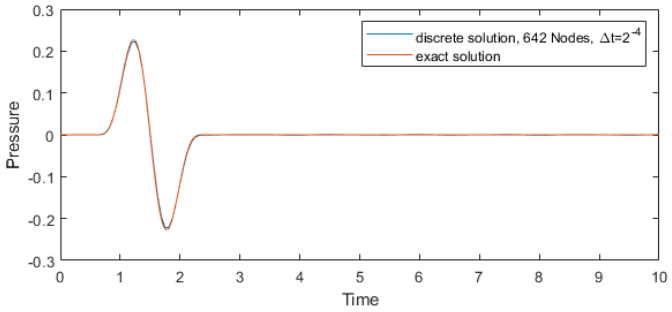

Fig. 2: Sound pressure at microphone point $x = (0, 1.5, 0)$.

to 10,242 nodes) using time steps from 2^{-1} to 2^{-6}. The relation between the time step size Δt and the spatial mesh size h is approximately $\Delta t/h \approx 0.38$. The six space-time meshes result in discretizations with between 240 and 6.55×10^6 degrees of freedom. Figure 2 presents the comparison between the computed and analytical sound pressure at the microphone location $x = (0, 1.5, 0)$, using a spatial mesh with $h = 0.15$ and a time step size of $\Delta t = 2^{-4}$.

Figure 3 illustrates the evolution of the absolute density error in the $\|\cdot\|_{L_2(\Gamma)}$-norm over time for the four finest space-time discretizations. As expected, the error decreases with a uniform refinement of the mesh size H, and it can be observed that the error remains uniformly. Figure 3 shows that halving the mesh size H leads to a reduction of the $\|\cdot\|_{L_2(\Gamma)}$-error by approximately a factor of 4, which corresponds to a quadratic convergence rate in H, consistent with Theorem 18 of [13].

Sound pressure signals are compared at several microphone points in the outer region of the upper quarter of the monopole

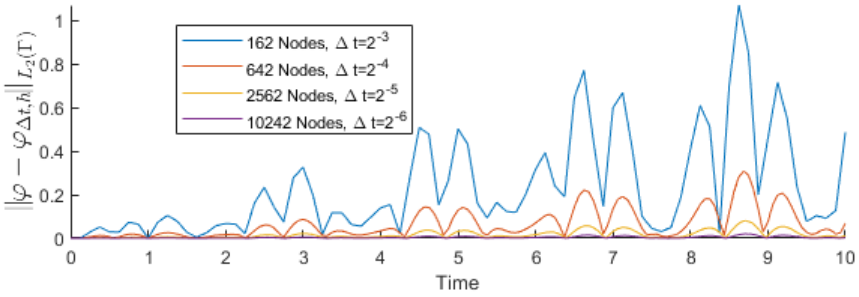

Fig. 3: $\|\psi - \psi_{\Delta t,h}\|_{L_2(\Gamma)}$ absolute error.

radiator (see Figure 1). To investigate the convergence behaviour in more detail, the relative errors of the density on Γ and the sound pressures at the microphone positions are evaluated over the time interval $T = [0, 10]$, using the following norms:

$$\frac{||\psi - \psi_{\Delta t,h}||_{L_2([0,10];L_2(\Gamma))}}{||\psi||_{L_2([0,10];L_2(\Gamma))}} \quad \text{and} \quad \frac{||u(t,x_i) - u_{\Delta t,h}(t,x_i)||_{L_2([0,10])}}{||u(t,x_i)||_{L_2([0,10])}}.$$

The overall pressure error is computed as the mean of the individual relative errors at all microphone positions. Figure 4 displays the relative errors for u and ψ with respect to the degrees of freedom. The observed convergence rate is approximately -0.70 for the sound pressure and $-2/3$ for the density. This is consistent with the quadratic convergence in H, taking into account that the number of spatial nodes scales quadratically and the number of time steps linearly with respect to the space-time degrees of freedom.

5 Numerical Investigation of Long-Time Stability

A key advantage of the $\mathcal{W}$-operator lies in its weak coercivity, compared to second-kind boundary integral formulations which ensures stability of the corresponding discrete space-time variational problem. In contrast, such stability results are not available for the $\mathcal{K}'$-operator due to its lack of coercivity, nor for collocation-based methods. This aspect is particularly relevant for practical applications, where simulations cover large time intervals or require very fine temporal resolutions to capture signals accurately. Here, we present numerical experiments that focus on long-time simulations, aiming to determine whether the favourable stability properties of the $\mathcal{W}$-operator are observed in computational practice. For this purpose, we

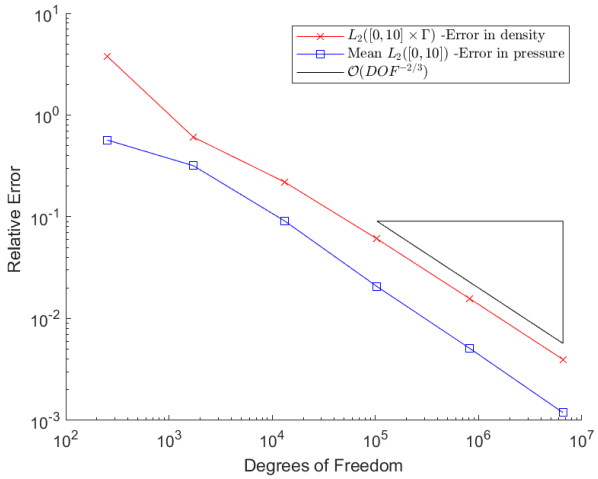

Fig. 4: Relative L_2 error of density and sound pressure.

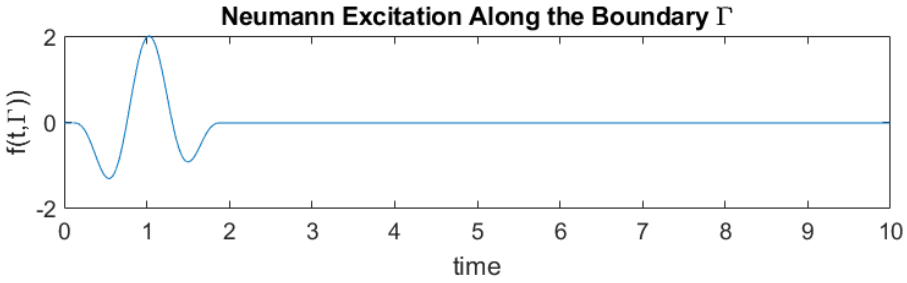

Fig. 5: Neumann boundary data used for the stability analysis.

compare the results to those obtained with the K'-operator, as discussed in [14], and with a collocation-based approach introduced in [17]. Our study considers a unit sphere discretized with 1280 elements and 642 nodes. We compute the density on Γ as well as the sound pressure at a microphone location $x_0 = (0, 1.5, 0)$, with the aim of assessing the stability of the solution over the time interval $[0, 6800)$. The time step sizes Δt are chosen so that the ratio $\Delta t/h$ takes the values $3.00,\ 1.50,\ 0.75,\ 0.38,\ 0.19,\ 0.10$, which corresponds to a range of $13,600$ to $452,200$ time steps. To specify the Neumann boundary condition f on $[0, 6800) \times \Gamma$, we employ the expressions given in equations (15) and (16). Thus, the boundary conditions are nonzero only within the time interval $0.1 < t < 1.9$, as illustrated in Figure 5. Unstable behavior is observed, although the Neumann boundary excitation is set to zero for all $t > 1.9$ s. We classify a simulation as unstable if its maximum computed density or sound pressure exceeds the corresponding analytical value by a factor of 100.

The results are illustrated in Table 1. For a more detailed insight, Figure 6 illustrates the results of all three methods for the

No.	$\Delta t/l_{\mathrm{El}}$	Δt	# timesteps	$\mathcal{W}$	K'	Colloc.
1	**3**	2^{-1}	13600	✓	✓	✓
2	**1.5**	2^{-2}	27200	✓	✗	✓
3	**0.75**	2^{-3}	54400	✓	✗	✓
4	**0.38**	2^{-4}	108800	✓	✗	✓
5	**0.19**	2^{-5}	217600	✓	✗	✓
5.1	0.16	$2^{-5.25}$	258771	✓	✗	✗
5.2	0.13	$2^{-5.5}$	307732	✓	✓	✗
5.3	0.11	$2^{-5.75}$	365958	✓	✗	✗
6	**0.10**	2^{-6}	435200	✓	✗	✗

Table 1: Stability Results for Different Grid Resolutions (Unit sphere).

$\Delta t/l_{\mathrm{el}}$ ratio of 0.1, showing detailed views over the first 4 seconds and up to 400 seconds.

The results demonstrate that, particularly for long simulation times, classical time-stepping approaches such as the collocation method become unstable for small space-time ratios (i.e., when $\Delta t/h < 0.16$). To analyze this in more detail, the time step size was further refined between $\Delta t = 2^{-5}$ and $\Delta t = 2^{-6}$ (cf. Table 1). In almost all simulations, the adjoint double-layer operator exhibited unstable behavior. Only discretizations No. 1 and 5.2 yielded stable results; however, these occurrences lack a systematic explanation and are therefore considered sporadic. In contrast, the hypersingular operator yields stable results across all simulations and throughout the entire considered time interval, regardless of the ratio $\Delta t/h$. This confirms

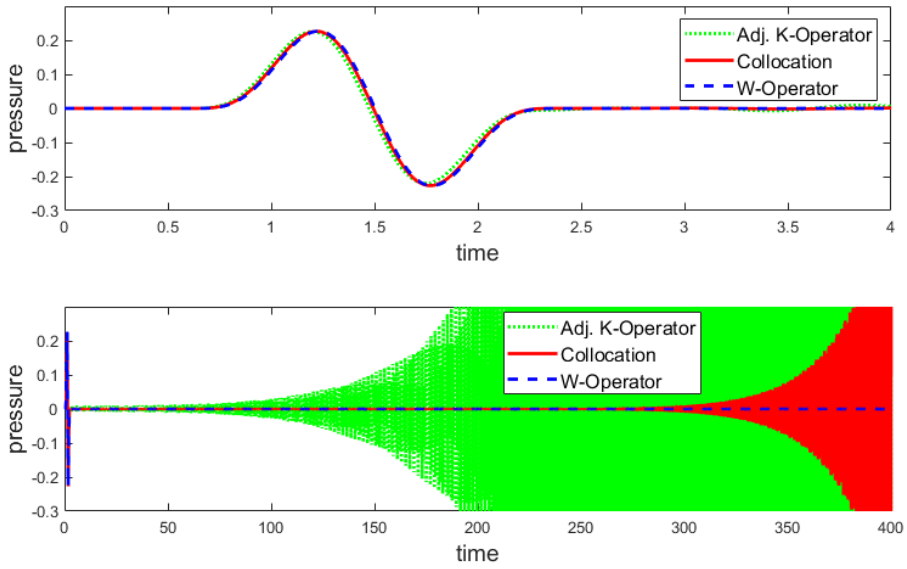

Fig. 6: Stability results for mesh no. 6 (Unit sphere): first 4 and 400 seconds.

the theoretical results from Section 2: the space-time formulation using the $\mathcal{W}$ operator allows stable simulations even for very long time intervals (more than 430,000 time steps), making it particularly suitable for practical NVH investigations.

6 Conclusions

This work presents a well-posed and numerically stable discretization of the hypersingular operator for the acoustic Neumann problem for the time-depended wave equation. The chosen trial and test functions yield a block lower-triangular structure of the system matrices, which enables efficient solution strategies based on block forward substitution, resulting in a time-stepping scheme. Numerical experiments confirm the stability of the formulation and demonstrate second-order convergence with respect to the size of the space-time elements. Extensive long-term simulations reveal stable behavior of the proposed formulation for all tested configurations. In contrast, a second-kind integral formulation and collocation approach shows a stability that depends on the relation between spatial and temporal discretization parameters. The discrete space-time variational formulation of the first-kind boundary integral equation permits independent choices of spatial and temporal mesh sizes due to its stability and well-posedness.
Future work will focus on understanding the stability and performance of the method for complex geometries and boundary conditions relevant to acoustic applications. Particular emphasis will be placed on signals with high-frequency ranges, which are especially important for practical applications and have not yet been sufficiently investigated.

Acknowledgements We appreciate the constructive discussions with A. Aimi and C. Guardasoni concerning the stability of second-kind boundary integral formulations.

References

[1] S. Schneider, B. Graf, M. Heinrich, T. Giese, and I. Haralampiev, *Practical application and validation of the time-domain boundary element method in acoustics*, in: Proceedings of ISMA2022 International Conference on Noise and Vibration Engineering, Leuven, Belgium, 2022.
[2] L. Banjai and F.-J. Sayas, *Integral Equation Methods for Evolutionary PDE*, Springer Series in Computational Mathematics, Springer, Cham (2022).
[3] M. Costabel and F.-J. Sayas, *Time-dependent problems with the boundary integral equation method*, Encyclopedia of Computational Mechanics, vol. 1, pp. 703–721, 2004.
[4] A. Bamberger and T. Ha-Duong, *Formulation variationnelle espace-temps pour le calcul par potentiel retard de la diffraction d'une onde acoustique*, Math. Meth. Appl. Sci., **8** (1986), 405–435 and 598–608.
[5] P. Joly and J. Rodriguez, *Mathematical aspects of variational boundary integral equations for time dependent wave propagation*, 2017.
[6] I. Terrasse, *Résolution mathématique et numérique des équations de Maxwell instationnaires par une méthode de potentiels retardés*, Thèse de doctorat, 1993.
[7] A. Aimi, L. Desiderio, and G. Di Credico, *Partially pivoted ACA based acceleration of the energetic BEM for time-domain acoustic and elastic waves exterior problems*, Computers & Mathematics with Applications, **119**, 351–370 (2022).

[8] D. Pölz and M. Schanz, *On the space-time discretization of variational retarded potential boundary integral equations*, Computers & Mathematics with Applications, **99**, 195–210 (2021).
[9] A. Veit, M. Merta, J. Zapletal, and D. Lukáš, *Efficient solution of time-domain boundary integral equations arising in sound-hard scattering*, International Journal for Numerical Methods in Engineering, **107**(5), 430–449 (2016).
[10] H. Gimperlein, M. Maischak, and E. P. Stephan, *Adaptive time domain boundary element methods and engineering applications*, Journal of Integral Equations and Applications, **29** (2017), 75–105.
[11] Stephan EP, Maischak M, Ostermann E (2008) Transient boundary element method and numerical evaluation of retarded potentials. In: Computational Science – ICCS 2008, pp 321–330. Springer, Berlin.
[12] E. Ostermann, *Numerical methods for space-time variational formulations of retarded potential boundary integral equations*, Ph.D. Thesis, Leibniz Universität Hannover, 2009.
[13] H. Gimperlein, F. Meyer, C. Özdemir, D. Stark, and E. P. Stephan, *Boundary elements with mesh refinements for the wave equation*, Numerische Mathematik **139**, 867–912 (2018).
[14] H. Gimperlein, C. Özdemir, and E. P. Stephan, *Time domain boundary element methods for the Neumann problem: Error estimates and acoustic problems* Journal of Computational Mathematics **36**, 70–89 (2018).
[15] F. J. Sayas, *Retarded Potentials and Time Domain Boundary Integral Equations: a Road-Map*, Springer, 2016.
[16] L. Banz, H. Gimperlein, Z. Nezhi, and E. P. Stephan, *Time domain BEM for sound radiation of tires*, Computational Mechanics, **58** (2016), 45–57.
[17] M. Stütz, *Stabilitätsverhalten und Anwendungen der transienten Randelementmethode in der Akustik*, Dissertation, Technische Universität Berlin, 2013.
[18] Ha-Duong T (2003) On retarded potential boundary integral equations and their discretisation. In: Topics in Computational Wave Propagation: Direct and Inverse Problems. Springer, pp 301–336
[19] A. Veit, *Numerical methods for the time-domain boundary integral equations*, PhD thesis, Universität Zürich (2011).
[20] H. Gimperlein, C. Özdemir, D. Stark, and E. P. Stephan, *A residual a posteriori error estimate for the time–domain boundary element method*, Numerische Mathematik **146**, 239–280 (2020).
[21] H. Gimperlein, Z. Nezhi, and E. P. Stephan, *A priori error estimates for a time-dependent boundary element method for the acoustic wave equation in a half-space*, Mathematical Methods in the Applied Sciences **40**(2), 448–462 (2017).